

Silk-based resorbable electronic devices for remotely controlled therapy and in vivo infection abatement

Hu Tao^{a,1,2}, Suk-Won Hwang^{b,1,3}, Benedetto Marelli^a, Bo An^a, Jodie E. Moreau^a, Miaomiao Yang^a, Mark A. Brenckle^a, Stanley Kim^b, David L. Kaplan^{a,c}, John A. Rogers^{b,d,e,4}, and Fiorenzo G. Omenetto^{a,f,4}

^aDepartment of Biomedical Engineering, Tufts University, Medford, MA 02155; ^bDepartment of Materials Science and Engineering, Beckman Institute for Advanced Science and Technology, and Frederick Seitz Materials Research Laboratory, University of Illinois at Urbana-Champaign, Urbana, IL 61801; ^cDepartment of Chemical and Biological Engineering, Tufts University, Medford, MA 02155; ^dDepartment of Chemistry, University of Illinois at Urbana-Champaign, Urbana, IL 61801; ^eDepartment of Electrical and Computer Engineering, University of Illinois at Urbana-Champaign, Urbana, IL 61801; and ^fDepartment of Physics, Tufts University, Medford, MA 02155

Edited by Margaret M. Murnane, University of Colorado, Boulder, CO, and approved October 20, 2014 (received for review May 5, 2014)

A paradigm shift for implantable medical devices lies at the confluence between regenerative medicine, where materials remodel and integrate in the biological milieu, and technology, through the use of recently developed material platforms based on biomaterials and bioresorbable technologies such as optics and electronics. The union of materials and technology in this context enables a class of biomedical devices that can be optically or electronically functional and yet harmlessly degrade once their use is complete. We present here a fully degradable, remotely controlled, implantable therapeutic device operating in vivo to counter a *Staphylococcus aureus* infection that disappears once its function is complete. This class of device provides fully resorbable packaging and electronics that can be turned on remotely, after implantation, to provide the necessary thermal therapy or trigger drug delivery. Such externally controllable, resorbable devices not only obviate the need for secondary surgeries and retrieval, but also have extended utility as therapeutic devices that can be left behind at a surgical or suturing site, following intervention, and can be externally controlled to allow for infection management by either thermal treatment or by remote triggering of drug release when there is retardation of antibiotic diffusion, deep infections are present, or when systemic antibiotic treatment alone is insufficient due to the emergence of antibiotic-resistant strains. After completion of function, the device is safely resorbed into the body, within a programmable period.

biomaterials | resorbable electronics | drug delivery | theranostics | silk

Implantable medical devices with increasing sophistication, such as those containing electronic components (1), are being developed for a variety of therapeutic or functions such as cardiovascular regulation, drug delivery, programmable therapy, or enhancement of biological structures (2). These devices are designed to operate while embedded in living tissue, which can lead to complications and restrictions on material constituents and form factors (3). Among the primary constraints are resistance to degradation while performing reliably and integration in the biological milieu without inflammatory response or rejection (4). Usually implantable medical devices provide mechanical and technological (e.g., electronic stimulators) functions largely based on stable, nondegradable materials that have finite operational lifetimes. These devices are first surgically inserted and eventually need to be retrieved or replaced once the desired functional outcome has been achieved or the useful lifetime of the device has ended (5, 6). This approach necessitates a secondary surgery, resulting in higher risks of postsurgical complications such as infection, inflammation, and pain (7), not to mention the disruption of the healed tissue. The lack of appropriate treatment of postoperative infections may cause severe problems including sepsis, organ failure, and even death (8).

Recent studies have demonstrated a class of completely water-soluble and fully resorbable silicon-based components (9), shedding light on biodegradable devices (10) with integrated functions that go well beyond those historically offered by resorbable sutures

(11), degradable intravascular stents (12, 13), and matrices for drug release (14, 15). A particular challenge for medical applications is how to externally control such devices and correlate this control with device degradation time, including the electronics and biomaterial support layers. Silicon and silicon oxide are typically used as active elements and passivation layers for resorbable electronics applications, and have relatively slow dissolution rates ranging from weeks to months, depending on temperature, pH, and thickness (9). Silk protein biomaterials have degradation rates that depend on crystallinity (e.g., beta-sheet content) and molecular weight of films used to support the electronic device. The lifetime of the devices can be specifically adjusted, chosen via the crystallinity of the silk (16, 17), yet operation in an in vivo environment imposes additional challenges because of mechanical handling, sterilization, and mechanical stability at the biopolymer–device interface.

Results and Discussion

For the present study, wirelessly controlled therapeutic devices were developed (Fig. 1). The materials used were Mg and MgO deposited onto silk substrates. Such devices exhibit fast dissolution times via hydrolysis (i.e., several hours, as opposed to weeks), once exposed to deionized (DI) water at room temperature (Fig. S1).

Significance

We present the demonstration of in vivo operation of a subcutaneously implanted, resorbable electronic device. The remotely controlled device was wirelessly activated after implantation, successfully eliminating infection, and subsequently dissolving in the surrounding tissue. This approach is a first step for the development of a class of implantable, technological, biomedical devices that resorb harmlessly, eliminating the need for retrieval after use.

Author contributions: H.T., S.-W.H., B.M., M.A.B., D.L.K., J.A.R., and F.G.O. designed research; H.T., S.-W.H., B.M., B.A., J.E.M., M.Y., M.A.B., and S.K. performed research; H.T., S.-W.H., B.M., B.A., J.E.M., M.Y., M.A.B., S.K., J.A.R., and F.G.O. analyzed data; and H.T., S.-W.H., B.M., D.L.K., J.A.R., and F.G.O. wrote the paper.

The authors declare no conflict of interest.

This article is a PNAS Direct Submission.

¹H.T. and S.-W.H. contributed equally to this work.

²Present address: State Key Lab of Transducer Technology, Shanghai Institute of Microsystem and Information Technology, Chinese Academy of Sciences, Shanghai 200050, China.

³KU-KIST, Graduate School of Converging Science and Technology, Korea University, Seoul 136-791, Republic of Korea.

⁴To whom correspondence may be addressed. Email: jrogers@uiuc.edu or fiorenzo.omenetto@tufts.edu.

This article contains supporting information online at www.pnas.org/lookup/suppl/doi:10.1073/pnas.1407743111/-DCSupplemental.

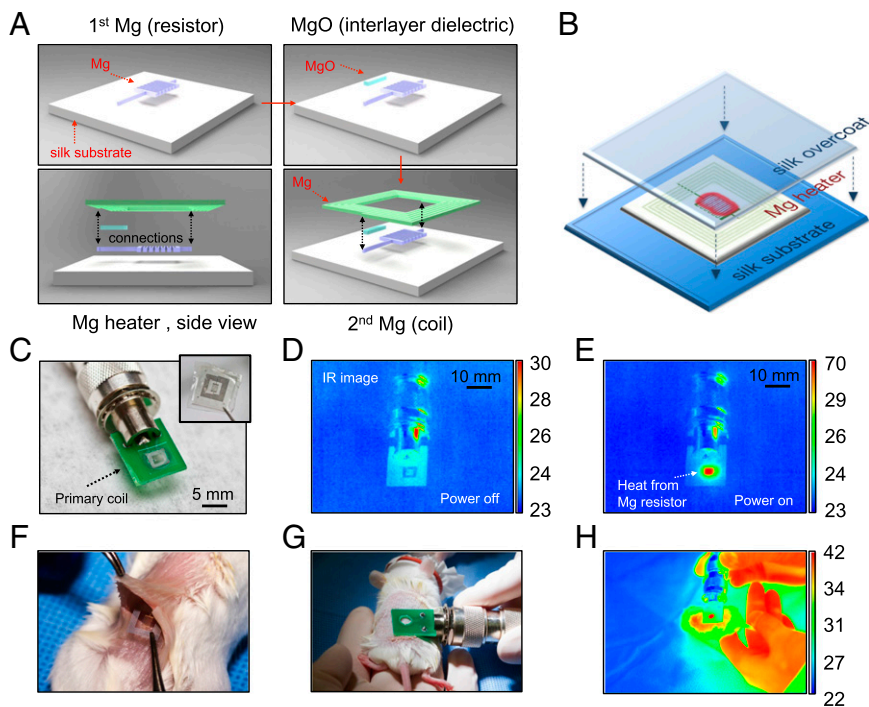


Fig. 1. Device fabrication and RF-thermal response characterization. (A) Fabrication procedure of the fully dissolvable wireless heating device consisting of a serpentine resistor and a power-receiving coil, both made of Mg, on a silk substrate. (B) The Mg heater was encapsulated in a silk “pocket” which protects the electronics and can be used to program the lifetime of the device. (C) The device can be remotely powered by being placed approximate to a primary coil through near-field coupling. Wireless inductive power transfer induces current flow in the circuit and heating of the resistor. (D and E) Thermal responses—power on and off—of the device are monitored using a commercial IR camera. (F and G) The device was implanted subcutaneously in a BALB/c mouse and was heated wirelessly. (H) Thermal image of the mouse with the device implanted (monitored in real time). Temperature scale bars, °C.

The lifetime of these devices can be further adjusted by using silk as an encapsulating material, allowing controlled rates of device dissolution ranging from minutes to weeks (*SI Text*). Before encapsulation, the device rapidly disintegrates in ~ 5 min and fully dissolves in ~ 150 min when immersed in DI water (Figs. S2 and S3). A series of *in vitro* (Fig. 1 C–E) and *in vivo* (Fig. 1 F–H) experiments was conducted to evaluate the wireless performance of the devices with a commercial IR camera (FLIR SC645, sensitivity: <0.05 °C). The local temperature of the heated area was continuously monitored by tuning the input power of the primary coil to maintain the temperature constant over 10-min intervals (i.e., the typical treatment duration). Temperature increases of $\Delta T_{in\ vitro} = \sim 47$ °C and $\Delta T_{in\ vivo} = \sim 20$ °C were corresponded to the position of the heater when the primary coil was operated at a wireless power of 500 mW at 80 MHz. The coupling efficiency was mainly determined by the geometries of the two coupling coils and their respective distance–alignment. The primary coil was aligned and placed on top of the implanted receiving coil with an approximate separation of 1 mm (i.e., mainly the skin of the mouse) to maximize energy transfer. A larger working distance of the order of the transmitting coil size is possible without significant decrease in coupling efficiency, although at a cost of higher input power (Figs. S4 and S5).

Functional performance of the wireless device to combat infection was evaluated *in vitro*, followed by *in vivo* studies in mice. An *in vitro* setup was used to explore the parameter space related to the therapeutic effectiveness of the device, specifically the effect of temperature and duration of heat treatment on bactericidal performance. The devices were placed underneath bacterial cultures of *Staphylococcus aureus* grown on agar plates (Fig. 2A). The IR heat map of the remotely activated device showed a central region with a sharp temperature differential of ~ 28 °C between the core (i.e., resistor) and the untreated areas (Fig. 2B) with

a power of 100 mW at 80 MHz. Higher temperatures can be obtained by adjusting the input radio frequency (RF) power in the primary coil. After treatment, the bacteria plates ($n = 6$) were immediately placed in a 37 °C incubator and examined the next day. The inhibition zones corresponded to the areas of heat treatment (Fig. 2C). Both power (thus temperature) and duration can be controlled to enhance bacterial inhibition (Fig. 2D).

Successful *in vivo* performance of this class of devices imposes a set of additional constraints such as their mechanical strength, resistance to handling, sterilization and implantation, and maintenance of function within the biological environment. The effectiveness of the device in this context was evaluated by the ability of the device to survive a surgical procedure, maintain its electronic functionality, and mitigate surgical-site infections. The studies were carried out in an animal model by adopting institutionally approved infection protocols. All animal experiments were conducted in accordance with approved Institutional Animal Care and Use Committee (IACUC) protocols at Tufts University. The wireless therapy devices were implanted in *S. aureus* infected BALB/c mice (Fig. 2E) at the infection site (Fig. S6). The devices were wirelessly activated for two sets of 10-min heat treatments with an input power of 100 mW (Fig. 2F) and 500 mW (Fig. 2G), which induced skin temperatures of 42 °C (labeled as “low temp”) and 49 °C (labeled as “high temp”), respectively. The measured temperatures were ~ 7 °C lower than the actual subcutaneous temperature (Fig. S7). The surgical sites were examined after 24 h to evaluate the effectiveness of the treatments (Figs. S8 and S9). Visual examination of the animals indicated effectiveness of the therapy revealing healing wounds. Further analysis was performed by excising the infected tissue site and assessing the normalized number of colony forming units (CFU) in the homogenate using

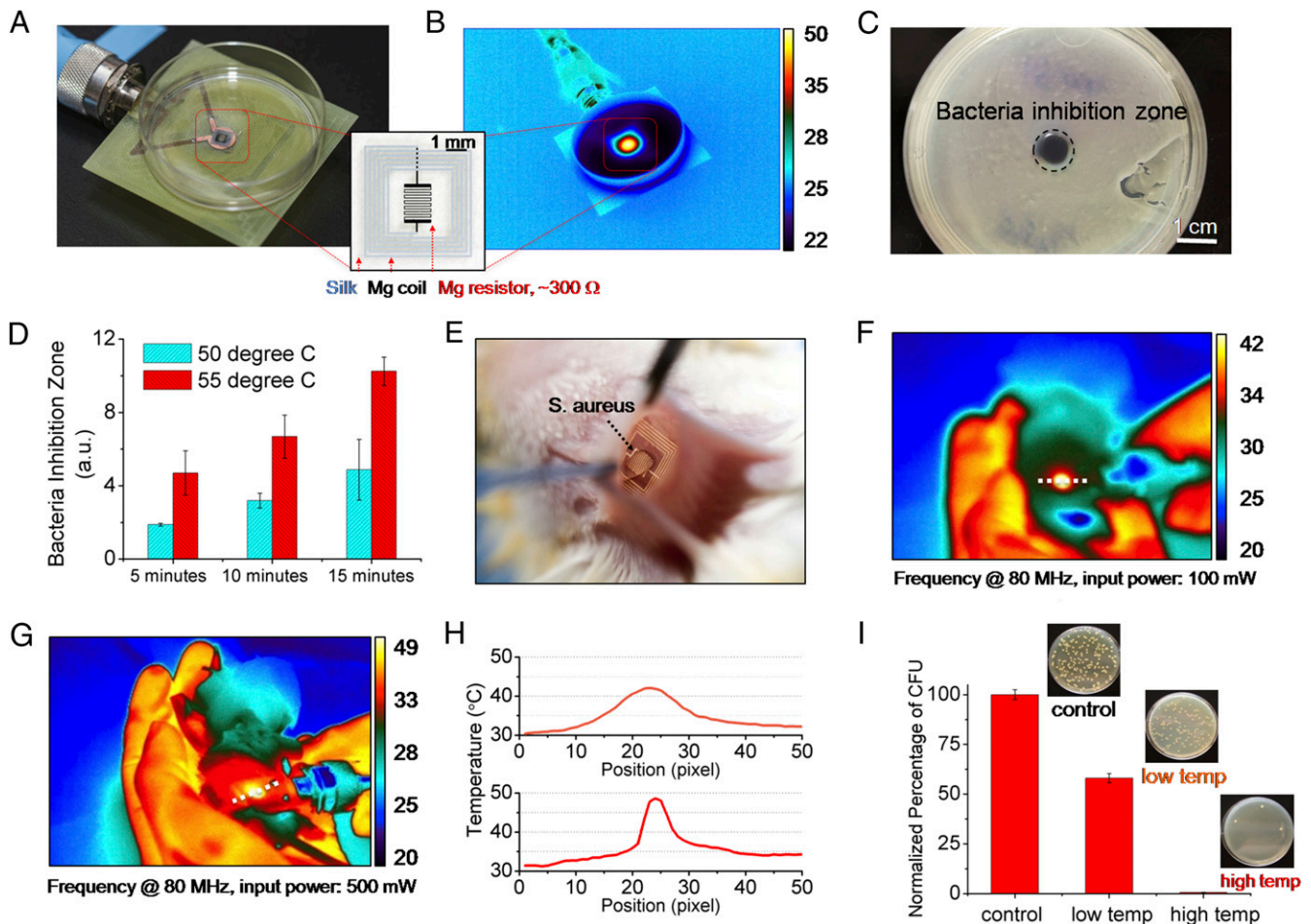


Fig. 2. In vitro and in vivo characterization of device performance. In vitro: (A) The devices were placed underneath bacterial cultures of *S. aureus* grown on agar plates. (B) The device was wirelessly powered to achieve a desired temperature, monitored by an IR camera. (C) A clear zone of inhibition, after heat treatment and overnight incubation, appeared in correspondence to the area of heat treatment application. (D) Increased power and thus temperature, and duration, enhance bacterial inhibition. In vivo: (E) Photo of a device implanted in BALB/c mice. The mice were infected with a subcutaneous injection ($\sim 5 \mu\text{L}$) of *S. aureus* at the device implantation site to mimic surgical-site infections. (F and G) Two sets of 10-min heat treatments (42 and 49 $^{\circ}\text{C}$, labeled as low temp and high temp, respectively) were carried out at a power of 100 and 500 mW after infection. (H) Measured temperature profiles corresponding to the two power levels used to remotely power the device. (I) The infected tissues were collected after 24 h and were assessed by counting the normalized number of CFU in the homogenates ($n = 3$) using standard plate counting methods.

standard plate counting ($n = 3$). A reduction in bacterial count was found for the thermally treated mice (Fig. 2H).

Eliminating the need to retrieve the device after its function is completed augments the appeal of external control of the device offered by wireless coupling. To accelerate in vivo assessments, resorbable devices that could be remotely (i.e., wirelessly) activated were designed for rapid degradation. The devices were sufficiently robust to survive mechanical handling during surgery, with degradation within a few hours after implantation (Fig. S8). Besides surgical-site infection experiments as described above, other functional devices were prepared to evaluate resorbability in vivo. These devices were implanted and postoperatively wirelessly activated in the subdermal region of two BALB/c mice (Fig. 3A). The animals were examined for traces of the device components at different time points. After 7 d, mouse 1 revealed faint residues of Mg inductive coils (originally $\sim 2 \mu\text{m}$ thick) supported on partially degraded silk substrates, with no evidence for the Mg serpentine resistor (originally $\sim 200 \text{ nm}$ thick) (Fig. 3B). Mouse 2 was examined after 15 d, which showed that the device was fully degraded with no visual evidence of any material residues (Fig. 3C). Tissue samples were collected from both the implantation site and from other locations surrounding the implant site

(labeled in Fig. 3 A–C) and analyzed to quantify residues. The normalized levels of residual Mg^{2+} ions in tissue sample homogenates were quantitatively determined using a commercial inductively coupled plasma atomic emission spectroscope (ICP-AES, Leeman Labs PS-1000). Mg levels in the surrounding tissues 15 d after implantation of the device approached physiological levels in tissues (18, 19) (Fig. 3D). Mg is abundant in the body as it is associated with more than 300 enzyme systems that regulate biochemical reactions, including muscle and nerve functions, blood sugar control, and blood pressure regulation (20). The total mass of Mg within each device was $\sim 27 \mu\text{g}$ (SI Text), a minimal quantity considering that the suggested daily intake of Mg for adults is $\sim 350 \text{ mg}$ (21). Histological sections also showed that the surrounding tissues were undisturbed by the treatment, underscoring the effectiveness of the device for localized thermal therapy (Fig. 3 E and F) and the effective dissolution of the conductive layers.

The biomaterials used are suitable for wireless therapeutic devices because of the ability of the device substrate to entrain stable therapeutic compounds. This property has been used extensively in silk biomaterials for drug stabilization and delivery (22). By designing the material composition (e.g., addition of

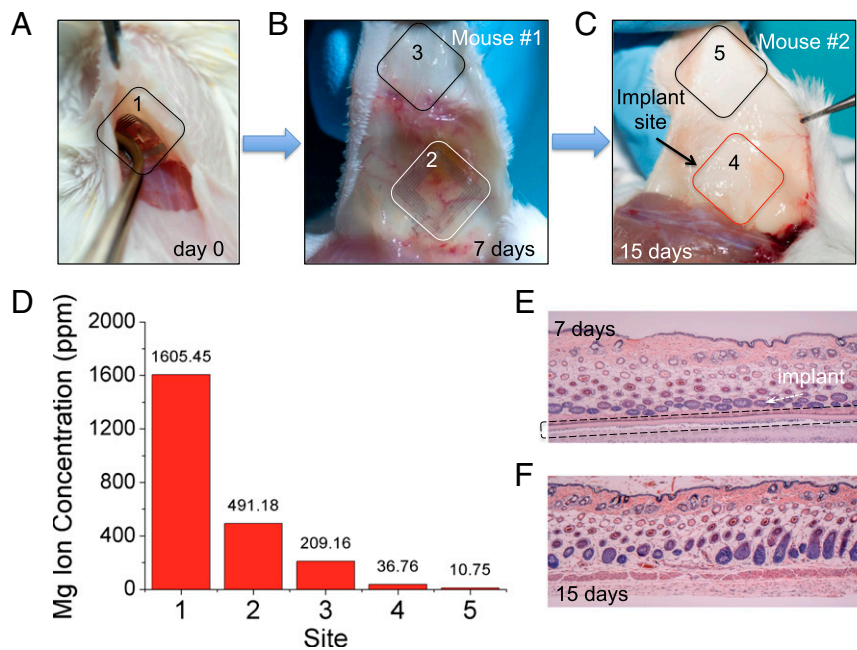


Fig. 3. Monitoring of device degradation and tracing of Mg ions. (A–C) Devices were implanted and examined after 7 and 15 days. (D) The normalized levels of residual Mg ions at different regions were determined and compared quantitatively. (#1 represents the initial amount of Mg on the day of implantation). Histological photos show that the device partially degraded in 7 d (E) and fully degraded after 15 d (F), without adverse inflammatory responses in the associated tissues.

drugs and/or enzymes to the silk material substrates) and the resorbable electronic interface, the devices can act as wireless drug delivery systems to offer programmable remote control of the release kinetics of a drug entrained and stabilized within the silk material matrix (Fig. 4A). This paradigm was tested in a

series of in vitro experiments in which an antibiotic was loaded in the silk films used for device fabrication, by mixing ampicillin solution with ~6 wt % silk solution (SI Text and Figs. S10–S12). The cast-and-peel process was used, as previously reported (23). All samples were treated to be water insoluble through a vapor

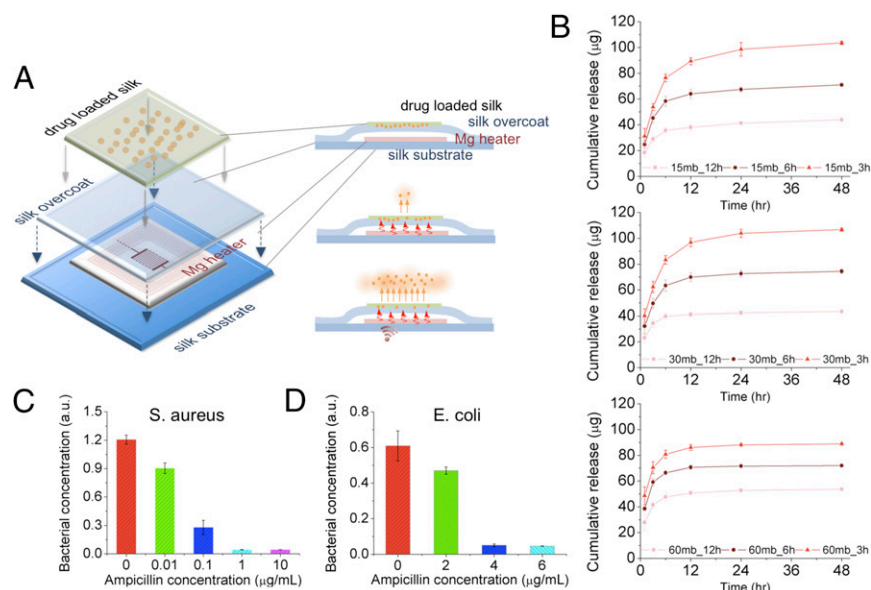


Fig. 4. In vitro characterization of antibiotic release profiles and bacterial inhibition upon heat treatment. (A) Schematic of the device integrated with antibiotics-doped silk film for wirelessly activated drug release. Ampicillin molecules loaded in silk films are illustrated as orange dots embedded in a green matrix. Antibiotic release from silk fibroin films was enhanced by increasing the temperature of the device with a wirelessly activated heater. (B) The cumulative drug release profiles (after application of thermal treatment at 50 °C for 10 min) were recorded. The release profile can be adjusted by controlling the boiling time (i.e., 15, 30, and 60 min, respectively) of raw silk fibers and water annealing time (i.e., 3, 6, and 12 h, respectively) of cast silk films for preferred crystallinity level. (C and D) Thermally triggered ampicillin release profiles were evaluated by adding the different ampicillin containing solutions into growth media containing *S. aureus* and *Escherichia coli* and subsequently measuring the optical density of grown bacterial cultures after 18 h of incubation at 37 °C.

annealing process (16, 17), which also helped to stabilize the drug within the crystallized silk matrix (24–26). Fig. 4B shows the cumulative release of ampicillin from silk films when wirelessly activated for 10 min. The results showed that silk solution extraction time (which impacts molecular weight) and water-vapor annealing (which impacts crystallinity), affected the antibiotic release kinetics. An increase in antibiotic release in the first 12 h was correlated with lower molecular weight silk (longer extraction time) and decreased exposure time to water-vapor annealing—or lower crystallinity. These results corroborate previously reported silk film drug-release profiles (27), where release kinetics was faster in silk films with decreased beta-sheet content and lower molecular weight. In addition, the release kinetics of ampicillin was enhanced by increasing the wireless driving power, corresponding to increased temperature for early time points ($t = 1, 3, \text{ and } 6 \text{ h}$) due to a combination of increased diffusivity of the antibiotic and temperature-driven annealing of wet silk chains which caused further crystallization. Additional strategies may be used at the time of film formation to further control and extend the release profile while maintaining the electronic interface. Exposure of antibiotic-loaded silk to

higher temperatures did not negatively affect antibiotic activity likely due to the stabilization properties of the silk on heat-labile compounds, as previously reported (25, 26).

Remotely controlled, resorbable therapeutic devices offer an expanded perspective for medical devices. The ability to control and wirelessly address therapy, whether thermal or biochemical, can enable broad operating windows with greater penetration depth than comparable noninvasive approaches. The results reported here focused on ampicillin release; however, approaches for broader applications in wireless drug release (ranging from small to large molecules entrained in silk) can be pursued based on this approach, even above body temperature (26). This would provide opportunities for externally controllable, therapeutic medical electronic devices that provide therapy-on-demand, followed by device resorption in the body.

ACKNOWLEDGMENTS. The authors gratefully acknowledge support from NSF-INSPIRE Grant (DMR-1242240), and from the NIH P41 (EB002520). M.A.B. would like to thank the American Society of Engineering Education for their support under the National Defense Science & Engineering Graduate Fellowship fellowship.

1. Ledet EH, et al. (2012) Implantable sensor technology: From research to clinical practice. *J Am Acad Orthop Surg* 20(6):383–392.
2. Grayson ACR, et al. (2014) A BioMEMS review: MEMS technology for physiologically integrated devices. *Proc IEEE* 92(1):6–21.
3. Irnich W (2002) Electronic security systems and active implantable medical devices. *Pacing Clin Electrophysiol* 25(8):1235–1258.
4. Anderson JM (2001) Biological responses to materials. *Annu Rev Mater Res* 31:81–110.
5. Stauffer RN (1982) Ten-year follow-up study of total hip replacement. *J Bone Joint Surg Am* 64(7):983–990.
6. Nery PB, et al. (2010) Device-related infection among patients with pacemakers and implantable defibrillators: Incidence, risk factors, and consequences. *J Cardiovasc Electrophysiol* 21(7):786–790.
7. Darouiche RO (2004) Treatment of infections associated with surgical implants. *N Engl J Med* 350(14):1422–1429.
8. Vogel TR, Dombrovskiy VY, Carson JL, Graham AM, Lowry SF (2010) Postoperative sepsis in the United States. *Ann Surg* 252(6):1065–1071.
9. Hwang SW, et al. (2012) A physically transient form of silicon electronics. *Science* 337(6102):1640–1644.
10. Tao H, et al. (2012) Implantable, multifunctional, bioresorbable optics. *Proc Natl Acad Sci USA* 109(48):19584–19589.
11. Lendlein A, Langer R (2002) Biodegradable, elastic shape-memory polymers for potential biomedical applications. *Science* 296(5573):1673–1676.
12. Peuster M, et al. (2001) A novel approach to temporary stenting: Degradable cardiovascular stents produced from corrodible metal—results 6–18 months after implantation into New Zealand white rabbits. *Heart* 86(5):563–569.
13. Moravej M, Mantovani D (2011) Biodegradable metals for cardiovascular stent application: Interests and new opportunities. *Int J Mol Sci* 12(7):4250–4270.
14. Hofmann S, et al. (2006) Silk fibroin as an organic polymer for controlled drug delivery. *J Control Release* 111(1–2):219–227.
15. Uebersax L, et al. (2007) Silk fibroin matrices for the controlled release of nerve growth factor (NGF). *Biomaterials* 28(30):4449–4460.
16. Hu X, et al. (2011) Regulation of silk material structure by temperature-controlled water vapor annealing. *Biomacromolecules* 12(5):1686–1696.
17. Lu Q, et al. (2010) Water-insoluble silk films with silk I structure. *Acta Biomater* 6(4):1380–1387.
18. Haigney MCP, et al. (1995) Noninvasive measurement of tissue magnesium and correlation with cardiac levels. *Circulation* 92(8):2190–2197.
19. Gomez MN (1998) Magnesium and cardiovascular disease. *Anesthesiology* 89(1):222–240.
20. Vormann J (2003) Magnesium: Nutrition and metabolism. *Mol Aspects Med* 24(1–3):27–37.
21. Yates AA, Schlicker SA, Suitor CW (1998) Dietary Reference Intakes: The new basis for recommendations for calcium and related nutrients, B vitamins, and choline. *J Am Diet Assoc* 98(6):699–706.
22. Omenetto FG, Kaplan DL (2010) New opportunities for an ancient material. *Science* 329(5991):528–531.
23. Tao H, et al. (2010) Metamaterial silk composites at terahertz frequencies. *Adv Mater* 22(32):3527–3531.
24. Lu S, et al. (2009) Stabilization of enzymes in silk films. *Biomacromolecules* 10(5):1032–1042.
25. Lu Q, et al. (2010) Stabilization and release of enzymes from silk films. *Macromol Biosci* 10(4):359–368.
26. Zhang J, et al. (2012) Stabilization of vaccines and antibiotics in silk and eliminating the cold chain. *Proc Natl Acad Sci USA* 109(30):11981–11986.
27. Pritchard EM, Valentin T, Panilaitis B, Omenetto F, Kaplan DL (2013) Antibiotic-releasing silk biomaterials for infection prevention and treatment. *Adv Funct Mater* 23(7):854–861.

Supporting Information

Tao et al. 10.1073/pnas.1407743111

SI Text

Methods. This involves a series of chemical-free processes including shadow mask deposition for the Mg resistor and coils, thin-film casting for the silk substrates, and low-temperature embossing (Fig. 1*A* and *B*). Briefly, the Mg serpentine resistor was fabricated on a silk substrate of $\sim 50\text{-}\mu\text{m}$ thickness with a resistance of $\sim 300\ \Omega$, determined by the metal thickness (i.e., $\sim 200\ \text{nm}$). After the deposition of MgO as a $1\text{-}\mu\text{m}$ passivation layer, a 6-turn receiving Mg coil ($\sim 2\ \mu\text{m}$) was deposited through a second deposition step to connect and power the serpentine resistor.

Materials. The bacteria strains used were *E. coli* and *S. aureus* ATCC 25923 (American Type Culture Collection). Bacterial culture dishes, BD brand Tryptic Soy Broth, and Tryptic Soy Agar were purchased from Fisher Scientific.

Silk Solution Preparation. Silk fibroin aqueous solutions were prepared as previously described. Briefly, *Bombyx mori* cocoons were boiled for certain period ranging from 15 to 60 min (varying with different applications and lifetime of devices), in an aqueous solution of 0.02 M sodium carbonate, followed by a thorough rinse using DI water. After 2 d drying in a chemical hood, the silk fibroin was dissolved in an aqueous solution containing 9.3 M lithium bromide at $60\ ^\circ\text{C}$ for 4 h. The solution was then injected in Slide-a Lyzer dialysis cassettes (MWCO 3500, Pierce) and was dialyzed against DI water for 48 h (8 water changing in an interval of 6 h). The final concentration of the silk fibroin was roughly 6 wt %, which was determined by drying 1 mL of as-prepared silk solution in an oven of $60\ ^\circ\text{C}$ overnight and measuring the weight of the final product–film. Molecular mass distribution: 171–460 kDa for 15-min boiled silk (15_mb); 31–268 kDa for 30-min boiled silk (30_mb); and 31–171 kDa for 60-min boiled silk (60_mb).

Silk Film Preparation. The silk solution was cast on a flat surface (i.e., the bottom of polystyrene Petri dishes) and was left drying at ambient conditions for 12 h, resulting in silk fibroin films. The thickness of silk film can be precisely controlled by adjusting the volume and concentration of the silk solution and the casting area. For example, a dose of $0.2\ \text{mL}/\text{cm}^2$ of 6 wt % silk solution produces films $\sim 100\ \mu\text{m}$ thick.

Ampicillin-Doped Silk Films Preparation. Sodium ampicillin (A9518, Sigma-Aldrich) was dissolved in MilliQ water (wt/vol = 50 mg/mL) at $4\ ^\circ\text{C}$ and then mixed with regenerated silk fibroin solution to obtain a solution made of 60 mg/mL silk fibroin and of 10 mg/mL sodium ampicillin. Antibiotic-loaded silk fibroin films (SF-AB) were then obtained by solvent casting.

Silk Film Postprocessing. Silk fibroin films are water-soluble. Certain processes can render the film water-insoluble. In this work, three methods were used. (i) Water annealing (for producing silk substrates on which the devices were fabricated): The silk films cast on silicon substrates (which were pretreated to be hydrophobic for easy peeling off after device fabrication) were placed in a water-filled vacuum desiccator. The vacuum pump was switched on for ~ 5 min to fill the desiccator chamber with vapor. The vacuum was then turned off to let the homogeneous water vapor anneal the silk films–samples. A minimum of 3 h vapor annealing was used to ensure the silk films did not dissolve in water. Longer annealing time increases the crystallinity within the films, resulting in slower degradation once implanted. (ii) Methanol annealing (for producing silk films for device encapsulation): The soluble silk

films were immersed in 80% (vol/vol) methanol solution for a certain period (ranging from 5 min to 1 h) to increase beta-sheet content within the films. (iii) Thermal annealing (for producing silk film for device encapsulation): The soluble silk films were thermal-treated using a house-built embosser. The embossing time, pressure, and temperature profile determine the crystallinity of the silk films, which determine the lifetime of the as-encapsulated devices.

Device Encapsulation Using Thermal Embossing–Lamination. Thermal embossing–lamination technique was used in this work for thermal control of silk fibroin film crystallinity. Moreover, with reflow upon heating, silk can act as a glue by controlling its thermal state.

Bacteria Culture. Lyophilized *S. aureus* and *E. coli* cultures were reconstituted and expanded according to instructions provided by ATCC. To test susceptibility, bacteria cultures were grown in liquid Tryptic Soy Broth for 18–24 h to an optical density (OD_{600}) between 0.8 and 1 (corresponding to a viable count of approximately 10^7 – 10^8 CFU per mL).

In Vitro Zone of Inhibition Testing. In vitro antibacterial effect was estimated by using the Kirby–Bauer Susceptibility Test, where antibacterial effect is assessed by comparing zones of clearance in bacterial lawns. Briefly, 50 μL of the *S. aureus* culture were plated on Tryptic Soy Agar plates. The devices were placed on a primary coil for wireless powering–heating. The heating temperature was controlled by adjusting the input power of the primary coil using an IFI Scx100 RF amplifier and a commercial IR camera (FLIR SC645). The treated plates were incubated overnight at $37\ ^\circ\text{C}$ to allow lawn growth. After 24 h the zone of inhibition was measured and analyzed using ImageJ image analysis software.

s.c. *S. aureus* Infection in Vivo Studies. Male BALB/c mice weighing 20–25 g were shaved on the back and depilated with Nair (Carter-Wallace Inc.). Mice were anesthetized with an injection of ketamine–xylazine mixture (90 mg/kg ketamine, 10 mg/kg xylazine) for surgery and infection. The operative area of skin was cleaned with alcohol, and the silk devices were implanted s.c. on the shaved back of each animal. Five μL of diluted bacteria culture containing $\sim 2 \times 10^5$ CFU of *S. aureus* were dropped on top of the silk devices and implanted together with the device. Wireless heating treatments were performed at different temperatures (42 and $49\ ^\circ\text{C}$) for 10 min. During the 10 min of thermal application the animals were kept under anesthesia. After 24 h, animals were anesthetized and tissues at the implantation site and surrounding area were excised and transferred to sterile 50-mL Falcon tubes containing 10 mL of sterile Dulbecco's phosphate buffered saline for further processing. The mice were then euthanized by carbon dioxide asphyxiation. All animal studies were conducted under protocols reviewed and approved by Tufts University IACUC protocols.

Tissue Homogenization and Bacteria Counting. Excised tissue samples were weighed and homogenized using a T25 basic Ultra Turrax mechanical homogenizer (IKA Works, Inc.). Bacteria in the homogenate were estimated by standard plate count methods. Colonies were counted after 24 h of incubation at $37\ ^\circ\text{C}$. The bacterial count was expressed as the number of CFU per wound. To normalize for variability among the mice, CFU counts for each treatment modality were divided by the CFU count measured for the untreated wound and reported as a percentage.

Antibiotic Release. Heat-stimulated ampicillin release was investigated as a function of silk fibroin molecular weight and polymorphic structure. To obtain silk fibroin with varying molecular mass, cocoon degumming time was set to 15, 30 and 60 min, to obtain protein with a molecular mass in the range of 171–460 kDa, 31–268 kDa, and 31–171 kDa, respectively (1). In addition, the degree of silk fibroin crystallinity was modulated to ~15%, 24%, and 33% by adjusting the time of the water-vapor annealing process to 3, 6, and 12 h, respectively (2). Antibiotic release from heat-stimulated silk films was then investigated by heating ampicillin-loaded silk films to 50 °C for 10 min in PBS (10 mg of film per mL of buffer) and then measuring ampicillin release adapting a previously reported protocol (1). In brief, 1 mL of PBS was added to each sample, which was then incubated at 37 °C. At desired time points (1, 3, 6, 12, 24, and 48 h), the buffer was removed and replaced with fresh buffer. The amount of released compound was determined using UV-vis spectroscopy at 230 nm. The amount of released antibiotic in each sample was summed with the amounts at each previous time point to obtain cumulative release values. Three samples were tested ($n = 3$) and each sample was assayed in triplicate.

Statistical Analysis. Antibiotic release data were compared with one-way ANOVA test with a Tukey means comparison implemented with software Origin Pro v.8 (OriginLab).

1. Pritchard EM, Hu X, Finley V, Kuo CK, Kaplan DL (2013) Effect of silk protein processing on drug delivery from silk films. *Macromol Biosci* 13(3):311–320.

Estimation of Mg Level of Each Device. The amount of Mg can be calculated based on design layout and thickness of a Mg heater. The calculated amount of Mg used for a resistor (~200 nm) and a spiral coil (~2 μ m) is 0.35 and 26.43 μ g, respectively, resulting in a total mass of Mg of 26.79 μ g.

Mg Ion Level Measurements Using ICP-AES. Freshly harvested mouse skin samples of similar dimension–weight were weighed, dried at 60 °C overnight, and then weighed again to determine the amount of dry solid mass in the tissue. Skin samples were then dissolved for 12 h in HCl 6M (Sigma-Aldrich). The same stock solution was used to dissolve all of the different samples to avoid possible interbatch difference in ion content. The Mg ion levels in each tissue were determined using ICP-AES (Leeman Labs PS-1000). A calibration test and a clean cycle were applied for each measurement to avoid cross-contamination.

Histology. To assess the safety of the heating procedure and the degradation process of the implanted devices, we examined histological slices of tissues surrounding the implanted devices. Samples were dehydrated through a series of graded alcohols, embedded in paraffin, and sectioned with slices having an approximate thickness of 10 μ m. Sections were stained with H&E.

2. Hu X, et al. (2011) Regulation of silk material structure by temperature-controlled water vapor annealing. *Biomacromolecules* 12(5):1686–1696.

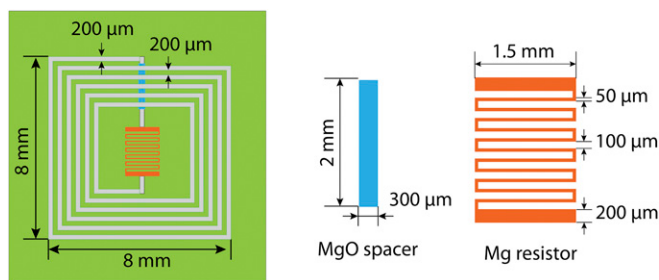


Fig. S1. Geometries and dimensions of the device used in the experiment.

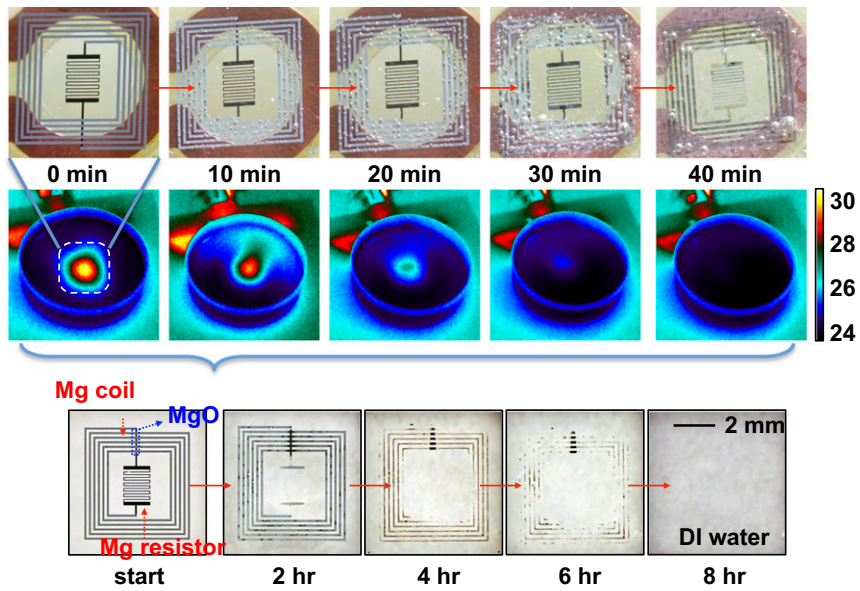


Fig. S2. Optical (and the corresponding IR) images of the dissolution of a device (consisting of a Mg serpentine resistor and a powering coil, fabricated on a glass substrate) in PBS at room temperature to illustrate the in vitro degradation process of individual Mg components.



Fig. S3. Optical images of full dissolution of the bare device (i.e., without any encapsulation layer) in DI water at room temperature over a time interval of 2.5 hours.

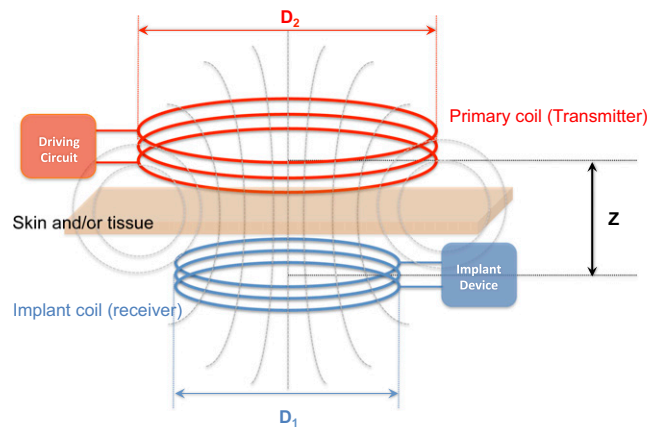


Fig. S4. Schematics of induction coupling between the primary coil and the receiver (i.e., implanted) coil for wireless power delivery.

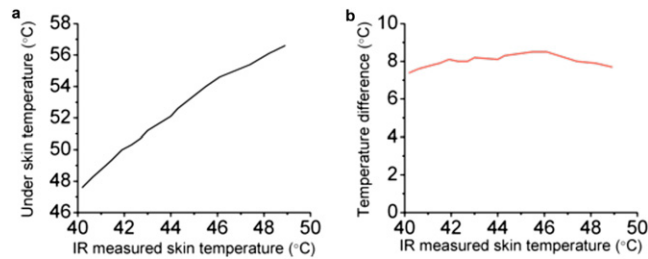


Fig. 57. Temperatures detected on the animal skin by the IR camera; the actual temperatures under the skin were measured to infer the actual temperature experienced at the implant site. The temperatures at the implant site were measured by using a thermocouple placed onto the device that was covered by a piece of mouse skin. The measured temperatures under the skin at the implant site were found to be $\sim 7^\circ\text{C}$ higher than the values recorded by the IR camera (i.e., skin temperatures).

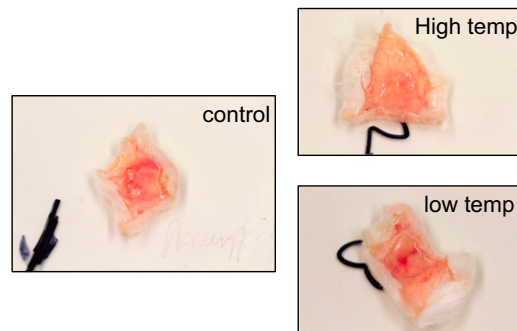


Fig. 58. Optical images of the excised tissues after the infection and thermal treatments. (Left) No thermal treatment was applied. Obvious infection as observed, as indicated by the presences of redness and pus. (Right, Top) Ten-min treatment at $\sim 57^\circ\text{C}$, labeled as high temp; no obvious signs of infection were found. (Right, Bottom) Ten-min treatment at $\sim 49^\circ\text{C}$, labeled as low temp; signs of infection were found, e.g., the presence of redness.

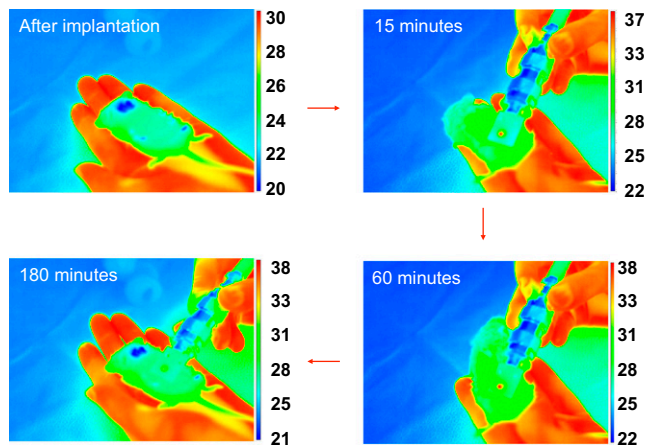


Fig. 59. IR images showing that the implanted device (for the assessments of the device degradation and Mg tracking purpose) started degrading within a time frame of 3 h, as indicated by a decrease of the device's thermal performance (i.e., temperature) when inductively activated by the same amount of RF power.

